

# Evolution of the crack network in glass samples submitted to brittle creep conditions

Celine Mallet · Jerome Fortin · Yves Guéguen · Frederic Bouyer

Received: 15 July 2014 / Accepted: 21 October 2014 / Published online: 9 November 2014  
© Springer Science+Business Media Dordrecht 2014

**Abstract** A crack network is introduced in glass by quenching heated samples. The sharp variation of temperature at the sample boundaries leads to tensile stresses that nucleate cracks. Then, they propagate in the entire sample. Quenching has been performed at 100, 200 and 300 °C. Cracks have been imaged with a scanning electron microscope. A transverse isotropic crack network is observed. Crack length and orientation have been measured. Obtained crack density has been compared to that inferred from elastic wave velocity measurements using effective medium theory. Cracked samples have been then submitted to creep tests. Two samples have been recovered, one before its failure and another after. Our observations show that vertical crack propagation takes place during brittle creep and that tertiary creep leads to a localized failure in a shear plane. The damaged and post-mortem microstructural networks have been documented.

**Keywords** Crack density · Damaged material · Crack network · Glass

## 1 Introduction

The interest of studying cracks in glass has been strong from the early beginning of fracture mechanical studies (Griffith 1921). Indeed, glass has a perfectly homogeneous and amorphous structure without porosity. Cracks are really easy to observe in this kind of material. In this study we used boro-silicate glass samples. Because of their manufacturing, some air bubbles are trapped in the glass matrix but the porosity is very small <1 %, and not connected. Cracks are introduced by quenching heated samples (Ougier-Simonin et al. 2011). The resulting crack network for a particular temperature (300 °C) has been previously investigated in this material (Mallet et al. 2013a). demonstrate that it is possible to directly measure the crack density from microstructural investigation in glass samples. They found for a 300 °C thermal treatment at global crack density of 0.05. They also observed an homogeneous crack network with a Transverse Isotropic (TI) symmetry.

The present work focuses on the evolution of the crack network with damage. Firstly, three crack networks are documented. They are introduced at different temperatures. Then, crack network of deformed samples are observed. Indeed, glass can deform under constant applied stress due to sub-critical crack propagation. This is the “brittle creep” regime (Atkinson 1984; Atkinson and Meredith 1987; Paterson and Wong 2005). In the second part of this study we observe the evolution of the crack network submitted to creep

---

C. Mallet (✉) · J. Fortin · Y. Guéguen  
Laboratoire de Géologie, Ecole Normale Supérieure,  
CNRS, UMR 8538, Paris, France  
e-mail: mallet@geologie.ens.fr

F. Bouyer  
CEA Marcoule, Bagnols-sur-Cèze, France

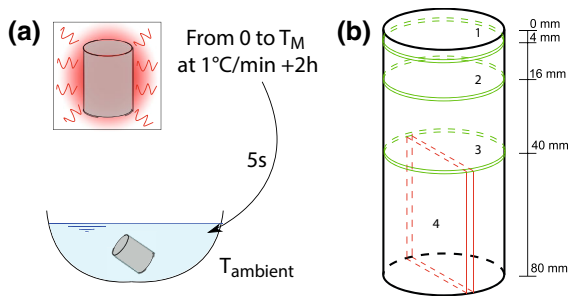


**Fig. 1** **a** Schematic view of the thermal treatment that introduces the initial crack network. **b** Four thin sections were cut in cracked glass samples in order to investigate the initial crack network

tests. The evolution of the entire crack network has been documented from observations after and before failure using Scanning Electron Microscopy (SEM). Two samples are investigated. The first one was recovered after secondary brittle creep damage and the second one after its failure in tertiary creep. During both creep tests, volumetric strain and Acoustic Emissions (AE) have been recorded in order to follow the sample damage and account for the crack propagation. Elastic wave velocities have been measured before recovering the samples to infer crack densities (Walsh 1965a, b).

## 2 Methodology

### 2.1 Samples and thermal cracking

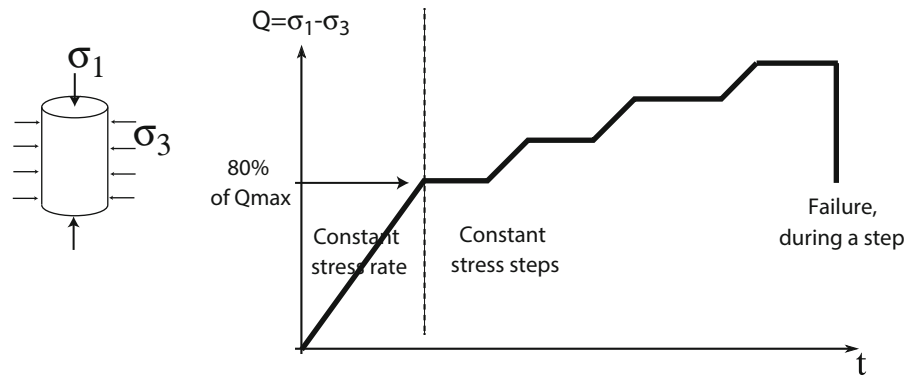
The original boro-silicate glass samples are produced in ideal conditions of slow cooling that prevents any crack formation. The reproducible method was developed by the French Atomic Energy Commission (CEA) laboratory (Marcoule). The glass is homogeneous and the porosity is about 1 % due to a few isolated air bubbles trapped in the glass matrix (this porosity is not connected). We used cylindrical specimens of 80-mm-length and 40-mm-diameter. Cracks were introduced by thermal shocks (Ougier-Simonin et al. 2011): samples were heated in an oven at 1 °C/min up to  $T_{max}$ . They were kept at this constant temperature during 2 h. Then, samples were quenched in less than 5 s in water at room temperature (Fig. 1a). Three temperatures,  $T_{max}$ , have been investigated: 100, 200 and 300 °C. Higher temperatures result in sample failure (Ougier-Simonin and Fortin 2010).

As a TI symmetry is expected for each  $T_{max}$  (Mallet et al. 2013a), four thin sections are cut in each thermally cracked samples in order to document the crack network, as in the schematic view of Fig. 1b: there are three horizontal sections. In these sections an isotropic crack distribution is expected to be in good agreement with the TI symmetry definition. The fourth section is cut in the lower half cylinder. It is a vertical section. Crack microstructure were imaged from the four thin sections, using a SEM. Images were obtained with a magnification of 60×. The mosaic picture of the entire surface was reconstituted by pasting images end to end.

### 2.2 Brittle creep experiments and sub-critical crack propagation protocol

Brittle creep in glass results of sub-critical crack propagation (Lawn and Wilshaw 1975; Ashby and Sammis 1990; Deshpande and Evans 2008; Bhat et al. 2011). The brittle creep experiments were performed using a conventional triaxial apparatus (axially symmetric:  $\sigma_2 = \sigma_3$ ) installed at the Laboratoire de Géologie in the Ecole Normale Supérieure in Paris. A more detailed description of this apparatus can be found in previous studies (Ougier-Simonin and Fortin 2010; Brantut et al. 2011). The confining pressure,  $P_c$ , is provided by a pump system using oil and can reach 100 MPa. During our experiments it is fixed at 15 MPa. The sample is isolated from oil by a neoprene jacket. The pore pressure,  $P_p$ , controlled by two independent pumps related to the top and the bottom of the sample, can reach 100 MPa. Pore fluid is a commercial mineral water in this study (to avoid any chemical exchange between glass and pore fluid), with a pore fluid pressure of 5 MPa. Thus the effective confining pressure is 10 MPa. The axial stress,  $\sigma_1$ , applied by a piston, can be increased up to 700 MPa for a 40-mm-diameter sample. During our creep tests we control the differential stress,  $Q = \sigma_1 - \sigma_3$ .

Volumetric strain was recorded during the brittle creep tests with strain gages. Also, 16 piezoelectric sensors are glued directly on the surface of the sample. In a passive mode, these sensors can record the AE that take place in the sample. The AE are amplified at 40 dB and discretely recorded (with a maximum record of 12 AE/s) (Thompson et al. 2005; Schubnel et al. 2007; Fortin et al. 2009). In an active mode, these sensors allow to obtain ultrasonic elastic wave veloc-

**Fig. 2** Creep experiment protocol

ities. Indeed, alternately sensors sent a pulse and the other ones recorded the transmitted wave.

The creep tests are performed following the protocol of stress-stepping (similar to that of [Heap et al. 2009a, b](#)). Hydrostatic pressure was first increased up to 15 MPa. Then, pore pressure was increased up to 5 MPa (water) and was kept constant during the experiment. In order to get a full saturation, the sample was maintained in these conditions for 2 days. Then, the axial stress path (Fig. 2) can be described in three stages. The first stage corresponds to an increase of the differential stress up to 80 % of  $Q_{\max}$  at a constant stress rate of 4 MPa/min. The maximum differential stress,  $Q_{\max}$ , is known from previous constant strain rate experiments performed on identical thermally cracked glass samples ([Ougier-Simonin and Fortin 2010](#)). When the loading reaches 80 % of  $Q_{\max}$ , the axial stress is maintained constant and the sample is allowed to deform under constant stress. This is the second stage and it corresponds to primary and secondary creep. The differential stress was kept constant for 24 h and then increased by 10 MPa. As a consequence, this second stage is the result of several steps of constant stress of 24 h each. This was repeated until failure occurred. The third stage is the last step when failure occurs in tertiary creep.

The mechanical behavior has been reported in [Mallet et al. \(2013b\)](#). This presented work is focused on crack microstructures: initial samples, recovered sample (at 95 % of  $Q_{\max}$ ) and post-mortem sample.

### 2.3 Crack density definition and measurement

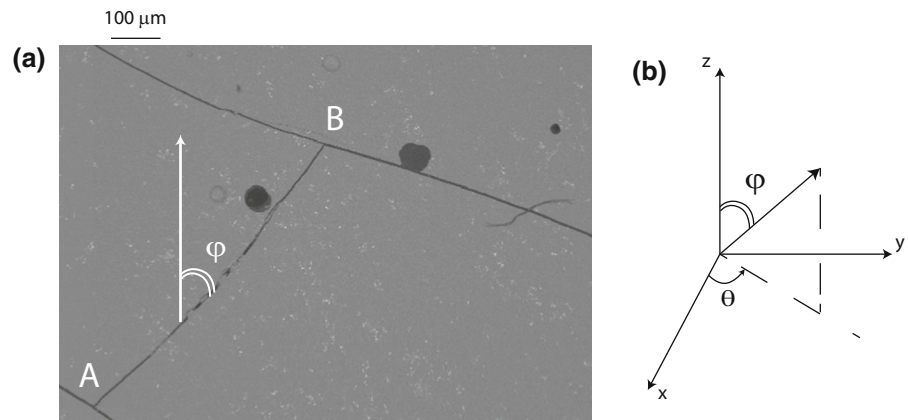
Crack density is a damage parameter introduced by [Bristow \(1960\)](#), to quantify the effect of cracks on elastic properties. It is defined as the ratio of the sum of all

the cubed crack radii versus the volume. Its value is  $\rho_c = \Sigma a_i^3 / V_T$ , where  $a_i$  is the radius of the  $i$ th crack and  $V_T$  is the total volume sample. [Kachanov \(1980\)](#) introduced the crack density tensor,  $\alpha$  described by its principal components:  $\alpha_1$ ,  $\alpha_2$  and  $\alpha_3$  that represent the crack density in the three orthogonal planes. In our case, a TI symmetry is assumed. It corresponds to  $\alpha_2 = \alpha_3$ .

From microstructural investigations, the two oriented crack densities ( $\alpha_1$  and  $\alpha_3$ ) can be obtained. All cracks radii are measured (they are assumed to be the half of the viewed crack length). Assuming a TI symmetry,  $\alpha_1$  and  $\alpha_3$  can be obtained from planar sections. Indeed, all of the horizontal cracks are intersected by a vertical section. On this section, the crack density of the horizontal cracks, represents the global horizontal crack density of the complete sample:  $\alpha_3$ . With the same consideration, all vertical cracks are intersected by horizontal sections. Thus the global crack density on these sections is the global vertical crack density of the complete sample:  $\alpha_1$ .

From elastic wave velocity measurements, crack densities can also be obtained. Elastic wave velocities of cracked samples have been measured in the tri-axial cell, before and during the creep experiments, with the 16 ultrasonic piezoelectric sensors ([Birch 1960](#); [Yin 1992](#); [Schubnel et al. 2006](#)). These sensors were glued at different orientations to get the velocity in different orientations ([Fortin et al. 2006](#)). This set of sensors allow to measure five velocities:  $V_P(90^\circ)$ ,  $V_P(45^\circ)$ ,  $V_P(0^\circ)$ ,  $V_{SV}(90^\circ)$ ,  $V_{SH}(90^\circ)$ . The angles are defined considering the axial axis of the cylinder as the  $0^\circ$ . Then, the effective compliance components are derived from the velocities. Assuming a TI symmetry, only five independent elastic constants have to be considered ([Guéguen and Kachanov 2011](#)). Compliance components,  $C_{ijkl}$ , are related to

**Fig. 3** a SEM image of cracks introduced by a thermal shock at 300 °C (vertical view). A crack is considered to be a single crack from one intersection (A) to another (B). Its radius is the half of segment AB. Its orientation is described on (b): crack normal is defined by two angles:  $\theta$  and  $\phi$



crack density through effective medium theory and the Non-Interaction Approximation (NIA) (Kachanov 1980; Guéguen and Kachanov 2011). Finally the effective compliance components derived from the velocities are inverted in terms of crack density component,  $\alpha_1$  and  $\alpha_3$ .

### 3 Initial crack network

#### 3.1 Imaging cracks in glass

Glass has a homogeneous structure, ideal for crack observations. SEM pictures show clearly cracks in glass (Fig. 3a). This picture is taken in a sample thermally cracked with  $T_{\max} = 300$  °C, on the vertical section (section 4 of Fig. 1b). In this SEM image, two kinds of heterogeneity are seen: bubbles (black dots) and cracks (thin lines). The bubbles can be filtered out. Then, with image processing (contrast treatment), cracks appear clearly, and a vectorial picture is obtained. The crack network can be imaged over the entire section. It is possible to measure, count and classify the cracks with respect to their orientation. A crack is assumed to be a single crack from one intersection (A dot on Fig. 3a) to another (B dot on Fig. 3a). The crack radius is the half of the viewed length (AB segment). Note that most cracks are linear, however some of them deviate from a straight line. We will assume in the following that if the deviation is smaller than a 10°-angle, the two branches are considered to be a single crack.

The orientation of cracks is defined on Fig. 3b. If the considered section is horizontal, the crack orientation is described with respect to the  $\theta$  angle. If the section

is vertical, it is described using  $\phi$  angle (Fig. 3a). The crack normal,  $n$ , is defined by angles  $\phi$ ,  $\theta$  (Fig. 3b)

#### 3.2 Microstructural observations: crack network induced by thermal shocks at 100, 200, 300 °C

The SEM mosaic of each of the four planar section of Fig. 1b is shown on Figs. 4, 5, 6. The crack network obtained after SEM image processing is shown in the central column. The corresponding projected crack density is shown in the last column. This last quantity corresponds to the total crack length measured on the image, per angle range of 45° (the crack plane is considered, not its normal). As an example, the value at the angle 360°/0° on section 4 represents the density of vertical cracks from vertical sections. On each figure, the three first subplots are the results for the three horizontal planes from the top to the middle of the sample, and the last subplot is for the vertical section taken in the lower half cylinder. Note that this section is doubled after image processing assuming a symmetry plane at the center of the sample (in order to get the complete vertical section).

The crack network microstructure of sample cracked at  $T_{\max} = 100$  °C, is represented on Fig. 4. The crack network shape can be described from the B column results. Boundaries effects are seen on section 1. Indeed, on this plane, cracks are more numerous and smaller than on sections 2 and 3. On the vertical section (4) there are a few long vertical cracks. There is no crack in the sample core. Looking at the oriented crack density (C column), we can see that it is very low (<0.002). Crack density decreases inside of the sam-

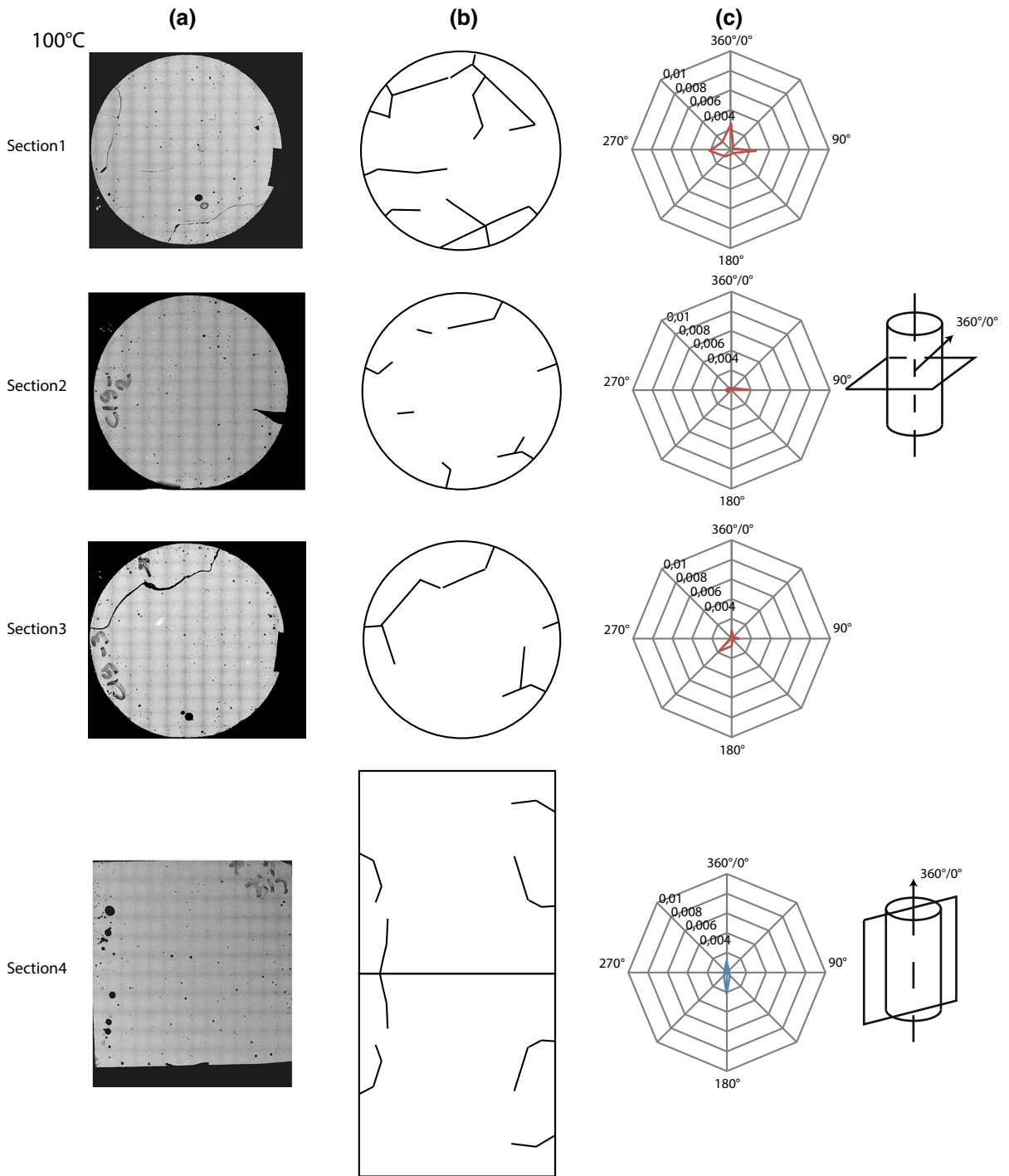


**Fig. 4** Initial crack network for a thermal shock of 100 °C. The *first column* is the mosaic sections of each thin section of Fig. 1b. The *second column* is the vectorized crack network. The *third*

*column* represents for each crack network the corresponding oriented crack density

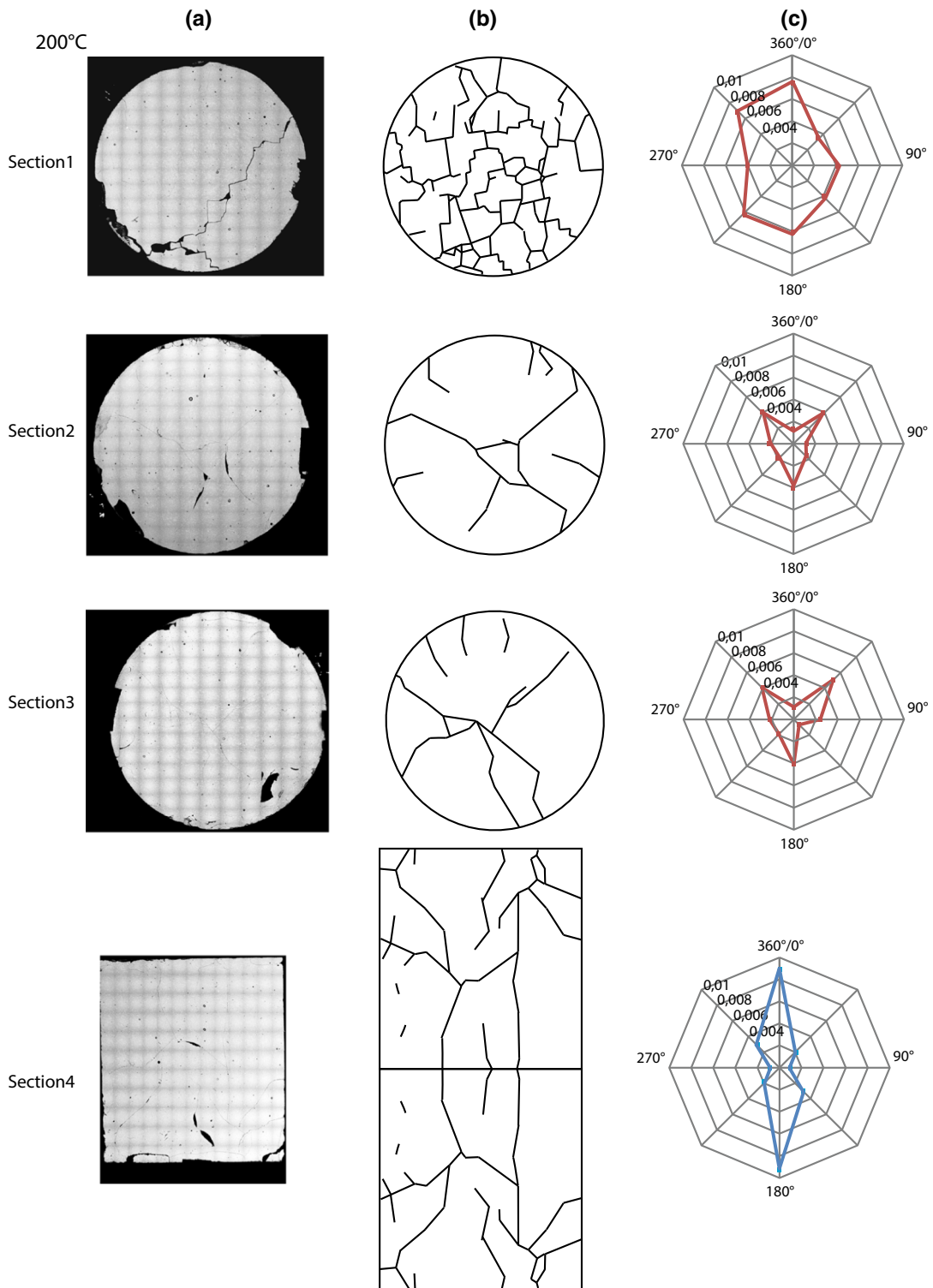


**Fig. 5** Initial crack network for a thermal shock of 200 °C. The *first column* is the mosaic sections of each thin section of Fig. 1b. The *second column* is the vectorized crack network. The *third*

*column* represents for each crack network the corresponding oriented crack density

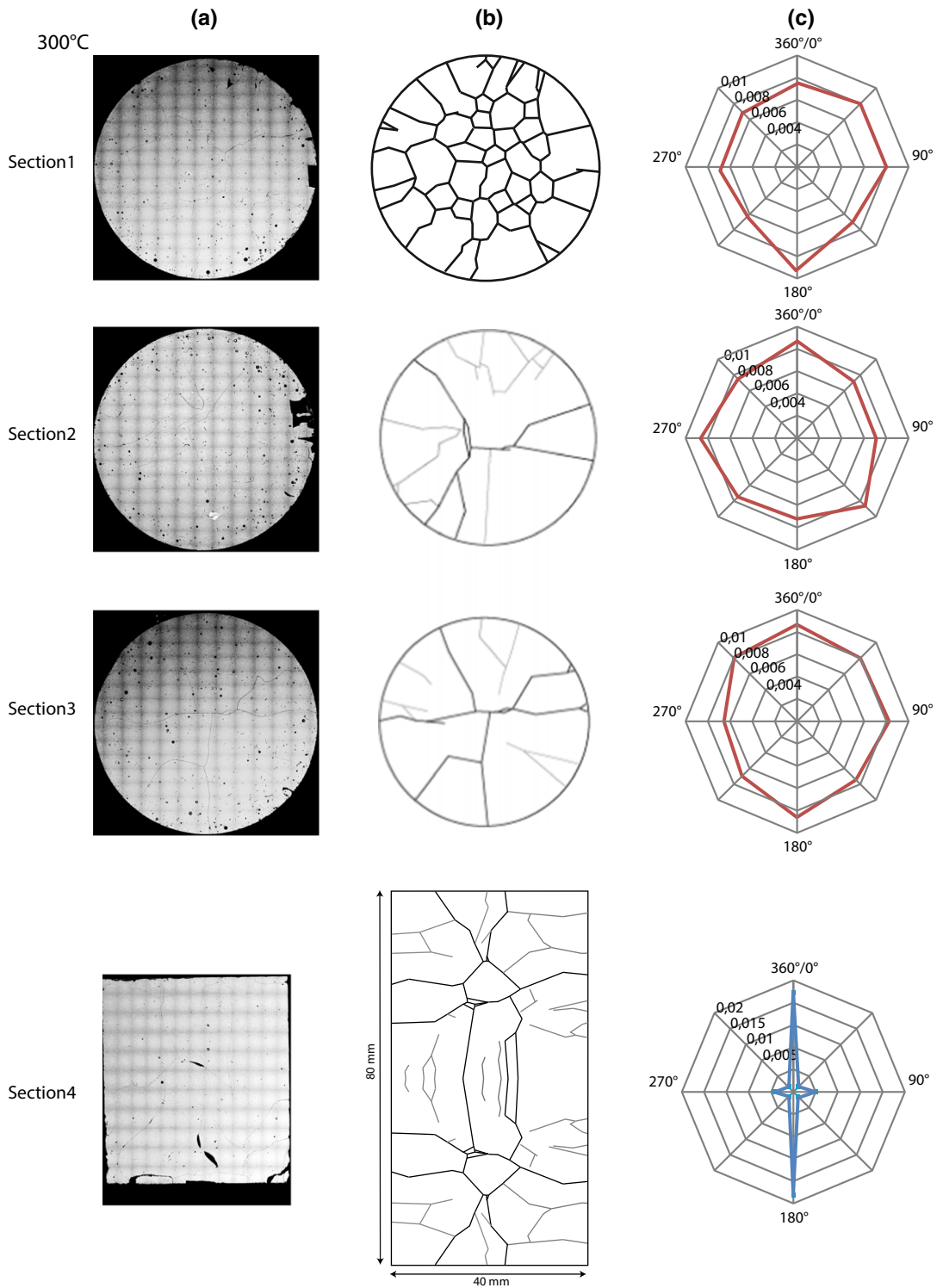


**Fig. 6** Initial crack network for a thermal shock of 300 °C. The *first column* is the mosaic sections of each thin section of Fig. 1b. The *second column* is the vectorized crack network. The *third*

*column* represents for each crack network the corresponding oriented crack density [modified from Mallet et al. (2013a, b)]

ple. On the vertical section, mostly vertical cracks are observed.

At  $T_{\max} = 200\text{ }^{\circ}\text{C}$ , the crack network is different (Fig. 5). Indeed crack density increases. The boundaries effects are more visible at this temperature: cracks are more numerous and smaller on section 1. An isotropic distribution of cracks is observed on the three radial planes. Crack density has the same value for section 2 and 3 (around 0.02) but is more important in section 1. On the vertical section (4) the long vertical cracks are very well observed. The crack density values are in good agreement with this observation.

Figure 6 represents the crack network of the sample cracked at  $T_{\max} = 300\text{ }^{\circ}\text{C}$ . The same boundaries effects are still present. However, on section 1, a hexagonal/pentagonal pattern is observed for the first section. Its symmetry is closed to the TI one. The vertical section shows some long vertical cracks. The oriented crack densities show that, from section 1 to 3, the crack density distribution is isotropic and has the same value. It indicates that in this last case, the crack network has a regular distribution up to the sample core. On the vertical section the anisotropy is clearly seen with the vertical crack predominance.

Considering that the vertical crack density of the whole sample is the average value of the crack density obtained from sections 1 to 3, and that the horizontal crack density is the value obtained with horizontal cracks present on section 4. Table 1 summarizes the results. Comparing the microstructural results of the three samples together with the crack density values, two points appear clearly. First some boundary effects are present and the crack network geometry is the same for the three samples. Indeed, the crack network of the first horizontal thin section (close to the cylinder top) is composed of smaller and more numerous cracks. On the radial sections an isotropic crack distribution is observed. The second point is that the average global crack density increases from a  $100\text{ }^{\circ}\text{C}$  thermal shock to a  $300\text{ }^{\circ}\text{C}$  thermal shock.

Moreover, cracks do not propagate up to the sample core for a thermal shock of  $100\text{ }^{\circ}\text{C}$  (Fig. 4), but they do propagate more deeply into the cylinder for shocks of 200 and  $300\text{ }^{\circ}\text{C}$ .

These two points allow to confirm the description of the crack network creation proposed by Mallet et al. (2013a, b). Tensile stresses (due to the sharp decrease of temperature at the cylinder boundaries) are responsible for crack nucleation. Then, with time, temper-

**Table 1** Crack densities from microstructural observations:  $\alpha_1$  (vertical cracks),  $\alpha_3$  (horizontal cracks) and global crack density,  $\rho_c (= \alpha_1 + 2\alpha_3)$ , for the initial samples cracked with three different temperatures

| Temperature | 100 °C | 200 °C | 300 °C |
|-------------|--------|--------|--------|
| $\alpha_1$  | 0.0056 | 0.021  | 0.041  |
| $\alpha_3$  | 0.0007 | 0.0016 | 0.0032 |
| $\rho_c$    | 0.007  | 0.024  | 0.047  |

ature decreases progressively up to the sample core and cracks propagate. Because only the  $300\text{ }^{\circ}\text{C}$  thermal shock, results in a constant crack density value through the entire sample, we will only consider this case for the following experiments.

#### 4 Crack network evolution resulting from brittle creep experiments

##### 4.1 Crack network of a thermally cracked sample deformed under secondary creep

The first considered creep test was performed with a glass sample thermally shocked at  $300\text{ }^{\circ}\text{C}$ . This sample was submitted to sub-critical crack propagation through brittle creep test. During this experiment, the confining pressure and the pore pressure are firstly set up (at 15 and 5 MPa, respectively). They will remain constant during the complete experiment. Then, the differential stress is firstly increased up to 225 MPa. Then, after 24 h, it was increased by 10 MPa. A succession of 10 steps was performed. At the end of the 10<sup>th</sup> step, failure in tertiary creep is not observed and the sample is recovered. This stress path is represented by the dashed line on Fig. 7a. This Figure shows also, the AE rate and the volumetric evolution during the succession of steps.

Note that for every step, the initial and secondary creep phases are always associated with a high level of AE rate. With the damage increase, the AE rate becomes more important and bursts of AE rate are more frequent. One particular step, at  $Q = 265\text{ MPa}$  is shown enlarged (Fig. 7b) to observe precisely the complete creep behavior during one step. The initial fast strain increase corresponds to primary creep. This is associated with a high level of AE rate (from 5 AE/s down to 1). The initial phase is followed by a second phase



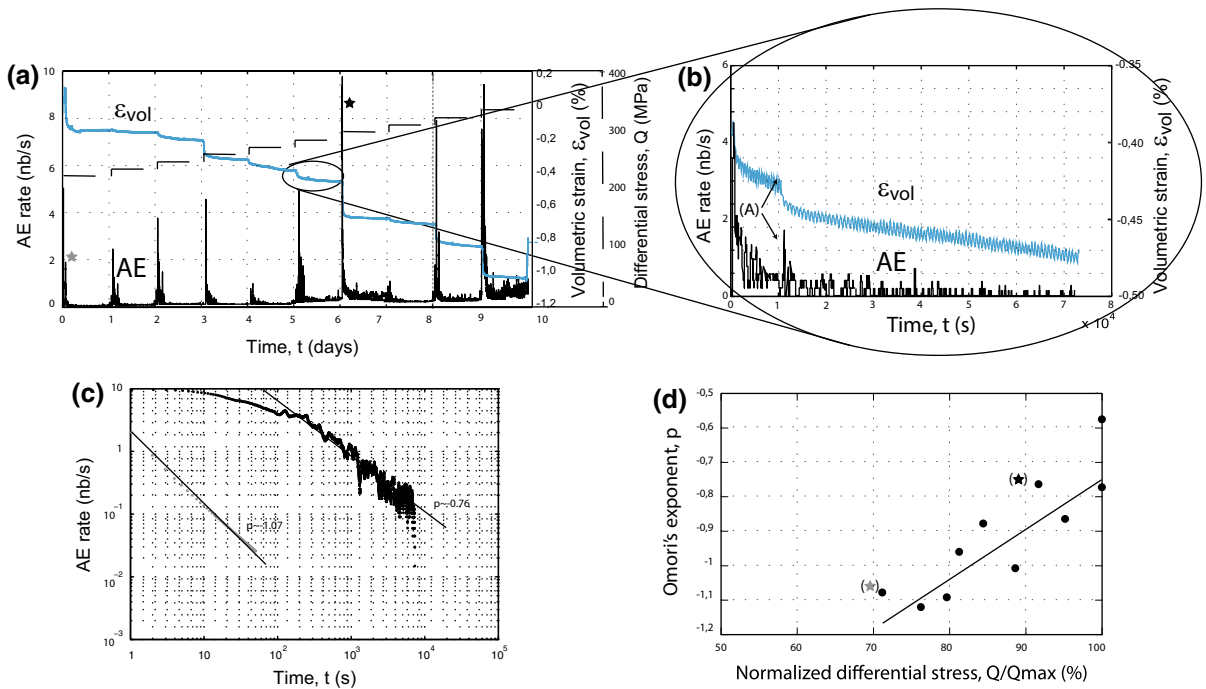


**Fig. 7** Observation of the Acoustic Emission (AE) rate and volumetric strain increase during the creep test. Confining pressure and pore pressure are fixed to 15 and 5 MPa, respectively. **a** Results from the complete experiment (differential stress in *dashed line* and cumulative volumetric strain in *blue line*). AE rate (*black line*) is observed to become more important close to the end of the experiment. **b** Zoom of **(a)**. Strain increases slowly

and a non-zero small AE rate is present. Strain jumps and AE bursts (A) are also observed. **c** Two bursts of AE noted with a star on **(a)** are reported using a logarithmic scale. Aftershocks follow a power law function with Omori's exponents of  $-1.09$  and  $-0.79$  for step 1 and 7, respectively. **d** Omori's exponents for all events reported versus normalized differential stress

where the volumetric strain seems to increase slowly and regularly. This is the secondary creep with a constant strain rate. In this second phase, the AE rate is constant around 1 AE/s. During the creep step, strain jumps can occur resulting in bursts of AE rate. An example of strain jump and AE burst is pointed by an arrow (A). Note that the volumetric strain (Fig. 7b) is characterized by very small oscillations of a period  $T = 6.10^{-4}$  s. These small oscillations are due to the regulation of the room and the cell temperature  $\pm 0.5^\circ\text{C}$ . Similar observations were reported in other granular materials (Divoux et al. 2008).

On Fig. 7a, two AE bursts are marked with a star. The grey one is on the first step (and it is one of the smallest burst), the black one highlights the most important AE burst (seventh step). These two AE events are observed on a logarithmic scale (Fig. 7c), that shows the number of aftershocks as a function of time. Both AE events follow a power law (Omori's law), with exponents of

$-1.07$  and  $-0.76$  for the first and the seventh steps, respectively. Finally, a similar observation can be done for each AE event and Fig. 7d represents the values of the Omori's exponents for the different stress values. An increasing trend is observed although scattering is important. This increase of the Omori's exponents with damage is similar to what has been reported on natural rocks such as porous sandstone (Ojala et al. 2003, 2004).

The sample was recovered before failure in tertiary creep, after the last creep step shown on Fig. 7. The SEM image of the complete vertical section is presented on Fig. 8a. Cracks are highlighted by image processing (Fig. 8b) and crack density is calculated (Fig. 8c). The resulting crack network shows important vertical crack propagation. Some horizontal cracks are observed. They were present in the initial state. An isotropic crack distribution (Fig. 8d) is observed on the radial plane indicating TI symmetry. From the vertical

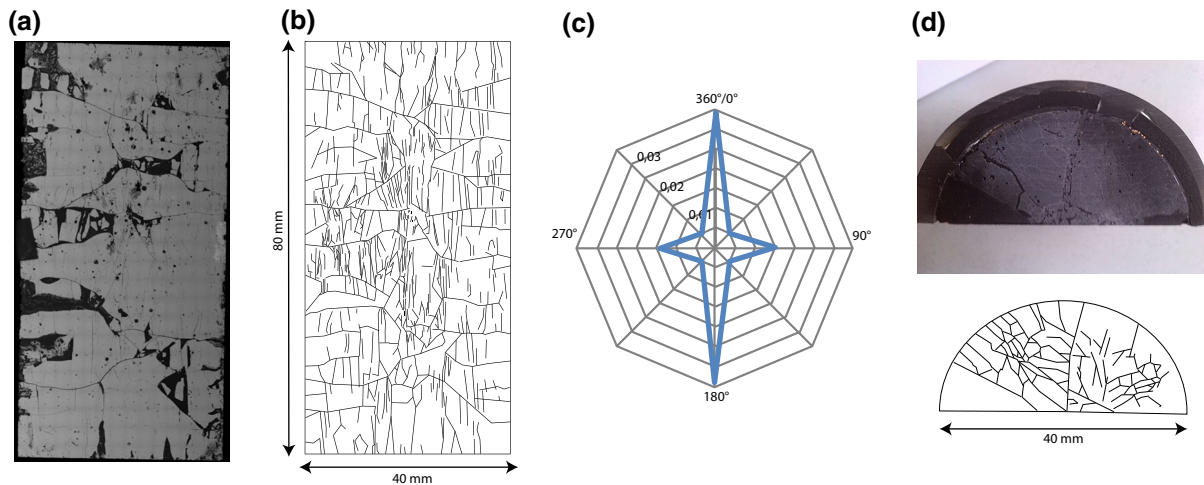


**Fig. 8** Sample recovered before its failure. **a** SEM picture of the complete vertical section. **b** Vectorized crack network of the entire vertical section. **c** Corresponding oriented crack density. **d** Picture of the horizontal half section and corresponding crack pattern

section, it is possible to obtain the horizontal crack density:  $\alpha_3 = 0.03$ . The vertical crack density,  $\alpha_1$ , could be measured from the radial sections:  $\alpha_1 = 0.20$ .

#### 4.2 Crack network of a thermally cracked sample after failure in tertiary creep

A second glass sample thermally shocked at 300 °C was submitted to sub-critical crack propagation through brittle creep test. The experimental conditions were the same as for the previous one (mineral water saturated condition, confining pressure of 15 MPa). During this experiment, the stress path is the same as previously but the sample failed in tertiary creep. The sample was recovered for microstructural observations. The last creep step is represented on Fig. 9. The volumetric strain and the AE rate are plotted. Three characteristic of a creep response are observed: in primary creep, a deceleration of strain is recorded with a high level of AE rate (at 12 event/s). During secondary creep, the strain rate is almost constant together with an AE rate that has decreased (and is about 1 event/s). During the tertiary creep an acceleration of strain is observed and the AE rate increases up to the failure. Note that during this last creep step, the failure occurs after 45 min.

Microstructural observations of the post-mortem cracks have been performed (Fig. 10). The post-mortem sample presents an oblique shear band where glass is crushed into powder. A thin layer of gouge is formed.

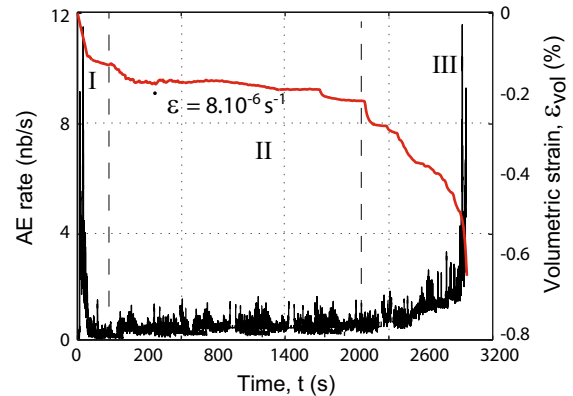


**Fig. 9** Volumetric strain and AE rate versus time during the last creep step. Primary, secondary and tertiary creep are separated by dashed lines

Two larger magnification images are shown: one outside the failure zone (Fig. 10b) and another from the failure zone (Fig. 10c). As in the previous sample, the initial horizontal cracks are still observable. These cracks present a pattern similar to that of the initial crack network (Fig. 6, central column, section 4). The failure zone appears to be a completely destroyed zone where glass is reduced into powder. The failure zone is a gouge of a 7 mm-thickness (Fig. 10c). Outside the failure zone, cracks are mainly vertical (Fig. 10b).

The crack pattern (Fig. 10d) allows to get crack density (Fig. 10e). From this vertical section, horizontal crack density is measured as,  $\alpha_3 = 0.044$ . A picture

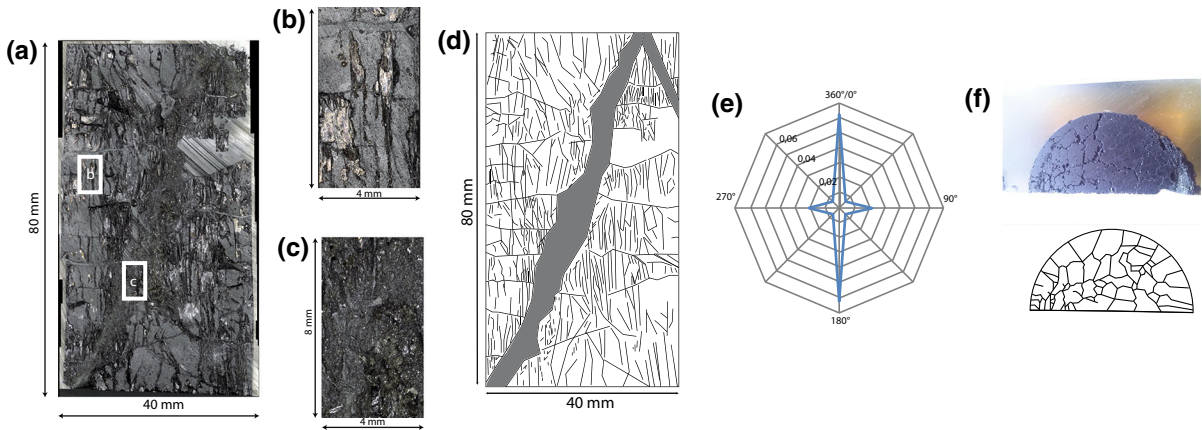


**Fig. 10** Post-mortem sample (after failure in tertiary creep). **a** SEM picture of the complete vertical section. **b, c** Zoomed views of cracks outside and inside of the failure zone. **d** Vectorized

crack network of the entire vertical section. **e** Corresponding oriented crack density. **f** Picture of the horizontal half section and corresponding crack pattern

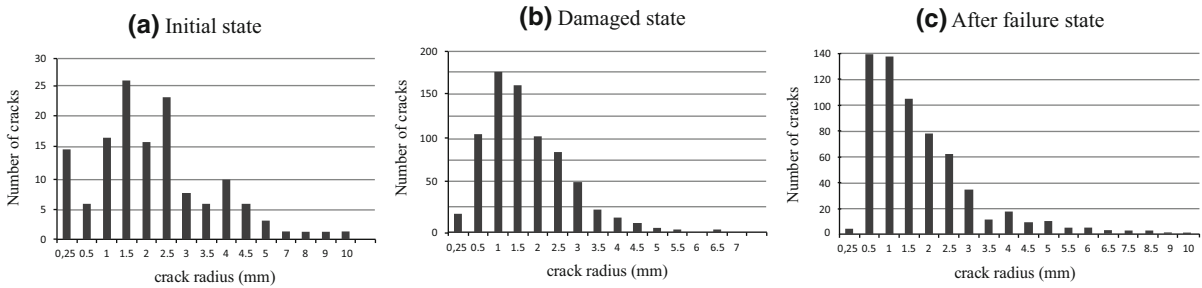


**Fig. 11** Crack radius histogram for **(a)** the initial state (sample thermally shocked at 300 °C), **(b)** the sample submitted to creep and recovered before failure, and **(c)** the post-mortem sample after failure in tertiary creep

of an half horizontal section (on the top of the cylinder) is also shown with its vectorized crack network (Fig. 10f). From this section, the vertical crack density is measured as,  $\alpha_1 = 0, 21$ . The crack density is closed to the crack density obtained in the previous case.

## 5 Discussion

### 5.1 Crack radius evolution with damage

On Fig. 11 is represented the histogram of crack radius of the initial cracked sample (at 300 °C, Fig. 11a), the damaged sample (section 6, Fig. 11b) and the post-mortem sample (section 7, Fig. 11c). From the initial, the damaged and the post-mortem samples, the maximal crack radii (around 10mm) remain constant. The statistical distribution of crack radii does not vary

strongly: in the three cases, the mean radius is around 1.8mm and the median radius is 3 mm. However the number of cracks is different. In the initial sample around 150 cracks are counted whereas 760 cracks are counted in the deformed sample. For the post-mortem sample we count almost 700 cracks but this excludes the crushed zone. We observe also that there are no more very small cracks. The distribution approaches an exponentially decreasing law.

The variation of the total crack’s number cannot be explained by the nucleation of new cracks. Indeed, the mechanical strength of uncracked glass is very high compared to that of the cracked glass ( $Q_{max} = 700$  MPa for uncracked glass and  $Q_{max} = 300$  MPa for a cracked sample at the same confining pressure of 15 MPa). Thus, crack nucleation cannot be expected in our creep test conditions. The apparent increase of crack’s number might be biased. To

**Table 2** Elastic wave velocities (m/s)

|                    | $V_P(90^\circ)$ | $V_P(45^\circ)$ | $V_P(0^\circ)$ | $V_{SV}(90^\circ)$ | $V_{SH}(90^\circ)$ |
|--------------------|-----------------|-----------------|----------------|--------------------|--------------------|
| Initial sample     | 6,100           | 5,950           | 5,750          | 2,980              | 2,900              |
| Damaged sample     | 5,900           | 5,250           | 4,950          | 2,150              | 1,950              |
| Post-mortem sample | 6,000           | 5,310           | 4,830          | 2,100              | 1,950              |

Measurements were performed for the initial sample thermally cracked at 300 °C and the two damaged samples. Crack densities were inferred from these measurements

**Table 3** Comparison of the crack density values calculated from microstructural observation and values inferred from elastic wave velocity results:  $\alpha_1$  (vertical cracks),  $\alpha_3$  (horizontal cracks) and global crack density,  $\rho_c$ , for the recovered samples

|            | Initial sample |          |           | Damaged sample |          |           | Post-mortem sample |          |           |
|------------|----------------|----------|-----------|----------------|----------|-----------|--------------------|----------|-----------|
|            | SEM            | Velocity | Error (%) | SEM            | Velocity | Error (%) | SEM                | Velocity | Error (%) |
| $\alpha_1$ | 0.041          | 0.038    | 7         | 0.20           | 0.25     | 25        | 0.21               | 0.27     | 28        |
| $\alpha_3$ | 0.0032         | 0.0034   | 6         | 0.03           | 0.038    | 27        | 0.044              | 0.06     | 36        |
| $\rho_c$   | 0.047          | 0.045    | 4         | 0.26           | 0.33     | 27        | 0.30               | 0.39     | 30        |

explain this observation, two interpretations are possible. The first one is to consider the crack propagation of initial micro-cracks that are not visible from SEM and from ultrasonic velocities. The initial sample could present the same crack number as those observed in the damaged samples, but many are too small to be measured. Probably, these cracks propagate. Thus, they are observed on damaged samples but not on initial sample. Another possible interpretation is that the increase of the crack's number is due to an increase of crack connectivity. Indeed, as cracks propagate, they intersect other cracks, leading to an apparent increase of the number of crack, due to our methodology (Fig. 3a). Crack branching and interconnectivity would then explain our observations.

It is however difficult to determine which interpretation is the appropriate one. The second explanation leads to consider that, using our crack length definition, a single crack can split into many, at least formally.

## 5.2 Crack density inferred from elastic wave velocities and from microstructural observation

From the five elastic wave velocity measurements, crack density can be inferred (see the framework of the work of Kachanov). Velocities are summarized in Table 2. The considered samples are the initial sample thermally cracked at  $T_{max} = 300$  °C, the damage

sample (secondary creep) and the post-mortem sample (tertiary creep).

For the initial sample, the comparison of the crack densities obtained from a direct and independent measurement (the microstructural observation) are really closed to the one inferred from the elastic wave velocities (Table 3). This good correspondence indicates that at this crack density level (around 0.05), the non interaction approximation is a good one.

For the two damaged samples, the crack density is higher (global crack density of  $\rho_c = 0.26$  and 0.30). In this case, it is observed that the elastic wave velocities lead to a different result. The discrepancy is of about 30%. A more reliable interpretation of this discrepancy is to consider that it highlights a threshold from which the non interaction approximation is no more valid. This threshold is consistent with the one determined by the previous study of Grechka and Kachanov (2006a; 2006b). In this study, the authors determinate that beyond a global crack density of 0.14, the non interaction method is no more exact.

## 6 Conclusion

Using SEM, cracks in quenched glass have been imaged and crack densities measured. The initial crack density is closed to 0.05 for a thermal chock at 300 °C. Cracks samples have been submitted to brittle creep

conditions. The experimental results show that brittle creep results from sub-critical crack growth. At constant stress, crack propagates up to a point where crack interactions take place and failure develops along an inclined shear plane. Failure takes place in tertiary creep and crack density increases up to 0.3.

From elastic wave velocity measurements, crack densities have been calculated through the non interactive approximation. At small crack density (around 0.05), this approximation is excellent. However, there is a threshold (crack density of about 0.3) beyond which the non-interaction approximation overestimates the crack density by 30%.

**Acknowledgments** We gratefully acknowledge our industrial partners AREVA NC and ANDRA for their financial support of this project. The authors thank the CEA-LCLT for fruitful discussion, for managing the whole project and for providing the glass samples.

## References

- Ashby M, Sammis C (1990) The damage mechanics of brittle solids in compression. *Pure Appl Geophys* 133(3):489–521
- Atkinson B (1984) Subcritical crack growth in geological materials. *J Geophys Res* 89(B6):4077–4114
- Atkinson BK, Meredith PG (1987) The theory of subcritical crack growth with applications to minerals and rocks. *Fract Mech Rock* 2:111–166
- Bhat H, Sammis C, Rosakis A (2011) The micromechanics of westerley granite at large compressive loads. *Pure Appl Geophys* 168(12):2184–2198
- Birch F (1960) The velocity of compressional waves in rocks to 10 kilobars, part I. *J Appl Mech* 65:1083–1102
- Brantut N, Schubnel A, Gueguen Y (2011) Damage and rupture dynamics at the brittle-ductile transition: the case of gypsum. *J Geophys Res* 116 (B01404). doi:[10.1029/2010JB007675](https://doi.org/10.1029/2010JB007675)
- Bristow J (1960) Microcracks, and the static and dynamic elastic constants of annealed and heavily cold-worked metals. *Br J Appl Phys* 11(2):81
- Deshpande V, Evans A (2008) Inelastic deformation and energy dissipation in ceramics: a mechanism-based constitutive model. *J Mech Phys Solids* 56. doi:[10.1016/j.jmps.2008.05.002](https://doi.org/10.1016/j.jmps.2008.05.002)
- Divoux T, Gayvallet H, Géminard JC (2008) Creep motion of a granular pile induced by thermal cycling. *Phys Rev Lett* 101(14):148–303
- Fortin J, Stanchits S, Dresen G, Guéguen Y (2006) Acoustic emission and velocities associated with the formation of compaction bands in sandstone. *J Geophys Res* 111(B10). doi:[10.1029/2005JB003854](https://doi.org/10.1029/2005JB003854)
- Fortin J, Stanchits S, Dresen G, Gueguen Y (2009) Acoustic emissions monitoring during inelastic deformation of porous sandstone: comparison of three modes of deformation. *Pure Appl Geophys*. doi:[10.1007/s00024-009-0479-0](https://doi.org/10.1007/s00024-009-0479-0)
- Grechka V, Kachanov K (2006) Effective elasticity of rocks with closely spaced and intersecting cracks. *Geophysics* 71(3):D85–D91
- Grechka V, Kachanov K (2006) Effective elasticity of fractured rocks: a snapshot of the work in progress. *Geophysics* 71(6):W45–W58
- Griffith A (1921) The phenomena of rupture and flow in solids. *Philos Trans R Soc Lond Ser A Contain Pap Math Phys Charact* 221:163–198
- Guéguen Y, Kachanov M (2011) Effective elastic properties of cracked rocks—an overview, in, *mechanics of crustal rocks*. CISM Courses Lect 533:73–125
- Heap M, Baud P, Meredith P (2009) Influence of temperature on brittle creep in sandstones. *Geophys Res Lett* 36(19). doi:[10.1029/2009GL039373](https://doi.org/10.1029/2009GL039373)
- Heap M, Baud P, Meredith P, Bell A, Main I (2009) Time-dependent brittle creep in darley dale sandstone. *J Geophys Res* 114(B7). doi:[10.1029/2008JB006212](https://doi.org/10.1029/2008JB006212)
- Kachanov M (1980) Continuum model of medium with cracks. *J Eng Mech Div* 106:1039–1051
- Lawn BR, Wilshaw R (1975) *Fracture of brittle solids*. Cambridge university press, Cambridge
- Mallet C, Fortin J, Guéguen Y, Bouyer F (2013a) Effective elastic properties of cracked solids: an experimental investigation. *Int J Fract* 181(2). doi:[10.1007/s10704-013-9855-y](https://doi.org/10.1007/s10704-013-9855-y)
- Mallet C, Fortin J, Guéguen Y, Bouyer F (2013b) Brittle creep and sub-critical crack propagation in glass submitted to triaxial conditions. *J Geophys Res* (in press)
- Ojala IO, Ngwenya BT, Main IG, Elphick SC (2003) Correlation of microseismic and chemical properties of brittle deformation in locharbriggs sandstone. *J Geophys Res* 108(2268). doi:[10.1029/2002JB002277](https://doi.org/10.1029/2002JB002277)
- Ojala IO, Main IG, Ngwenya BT (2004) Strain rate and temperature dependence of Omori's law scaling constants of AE data: implications for earthquake foreshock–aftershock sequences. *Geophys Res Lett* 31(24). doi:[10.1029/2004GL020781](https://doi.org/10.1029/2004GL020781)
- Ougier-Simonin A, Fortin J (2010) Cracks in glass under triaxial conditions. *Int J Eng Sci* 49:105–121
- Ougier-Simonin A, Guéguen Y, Fortin J, Schubnel A, Bouyer F (2011) Permeability and elastic properties of cracked glass under pressure. *J Geophys Res* 116. doi:[10.1029/2010JB008077](https://doi.org/10.1029/2010JB008077)
- Paterson MS, Wong TF (2005) *Experimental rock deformation—the brittle field*. Springer, Berlin
- Schubnel A, Walker E, Thompson B, Fortin J, Guéguen Y, Young R (2006) Transient creep, aseismic damage and slow failure in Carrara marble deformed across the brittle-ductile transition. *Geophys Res Lett* 33. doi:[10.1029/2006GL026619](https://doi.org/10.1029/2006GL026619)
- Schubnel A, Jones G, Thompson B, Fortin J, Guéguen Y, Young R (2007) Fluid-induced rupture experiment on Fontainebleau sandstone: premonitory activity, rupture propagation, and aftershocks. *Geophys Res Lett* 34. doi:[10.1029/2007GL031076](https://doi.org/10.1029/2007GL031076)
- Thompson B, Young R, Lockner D (2005) Observations of premonitory acoustic emission and slip nucleation during a stick slip experiment in smooth faulted westerly granite. *Geophys Res Lett* 32. doi:[10.1029/2005GL022750](https://doi.org/10.1029/2005GL022750)

- 
- Walsh J (1965) The effect of cracks on the uniaxial elastic compression of rocks. *J Geophys Res* 70(2):399–411
- Walsh J (1965) The effect of cracks in rocks on Poisson's ratio. *J Geophys Res* 70(20):5249–5257
- Yin H (1992) Acoustic velocity and attenuation of rocks: isotropy, intrinsic anisotropy, and stress-induced anisotropy. PhD thesis, Department of Geophysics, School of Earth Sciences, Stanford University